



Influence of yolk-shell Au@TiO₂ structure induced photocatalytic activity towards gaseous pollutant degradation under visible light

Yunyang Wang¹, Changzhu Yang¹, Ayan Chen, Wenhong Pu, Jianyu Gong*

School of Environmental Science and Engineering, Huazhong University of Science and Technology, Wuhan, 430074, China

ARTICLE INFO

Keywords:

Yolk-shell Au@TiO₂
Gaseous toluene
Photocatalytic oxidation
Morphology difference

ABSTRACT

Core-shell and yolk-shell Au@TiO₂ NPs were successfully synthesized, and the morphology differences were observed. Its photocatalytic activity was evaluated by photocatalytic oxidation of gaseous toluene under visible light illumination. The results indicated that yolk-shell Au@TiO₂ exhibited superior photocatalytic properties and demonstrated a good stability. Almost 57.3% of gaseous toluene was removed over 0.14 at% yolk-shell Au@TiO₂ in 3 h. It could also be reused for several times without corrosion. Furthermore, the comprehensive effect of LSPR response of Au, high cavity volume of yolk-shell structure, larger specific surface area, more mesoporous and the existence of Ti³⁺ were all benefit for the photocatalytic process. ESR tests also confirmed that h⁺, ·OH, ·O₂⁻ and Ti³⁺ generated from yolk-shell Au@TiO₂ were the main active species in the photocatalytic degradation progress of gaseous toluene under visible light irradiation.

1. Introduction

Volatile organic compounds (VOCs) are a group of gases that have serious impact on environmental quality and human health [1,2]. They could be emitted from furniture, decorations, construction products, industrial facilities and chemical industrial processes [3–5]. They are not only harmful compounds itself, but also can occur photochemical reactions with other atmospheric pollutants and produce secondary pollutants such as ozone [6]. A cyclic chain reaction will take place between some halogenated hydrocarbons and O₃, which will damage the ozone layer. At the same time, VOCs are also the main precursor of PM_{2.5} and the secondary organic aerosol (SOA) [7,8]. For example, formaldehyde (HCHO), benzene and phenol have carcinogenicity and teratogenicity for human [9] and strong photochemical activity in haze formation [10,11]. Gaseous toluene, a typical VOC, could accumulate in human's adipose tissue, liver and brain by entering the bloodstream through lung, skin and gastrointestinal tract [12,13]. In recent years, many advanced technologies for quick and complete removal of VOCs have been developed continuously [14–16], such as adsorption, photocatalytic oxidation, thermal oxidation and biofiltration, etc. Among them, photocatalytic oxidation is an innovative and promising approach due to its environmentally friendly products of carbon dioxide and water [17–19].

Among many kinds of photocatalysts, titanium dioxide (TiO₂) has

been widely studied as an environmental restoration photocatalyst due to its advantages of low cost, photochemical stability and strong oxidation property [20–22]. Until now, TiO₂ works as a photocatalyst that has been widely evaluated in remediation of polluted environmental because of its excellent photoelectricity transformation ability and photosensitive effect [23]. However, TiO₂ has a large band gap ($E_g = 3.2$ eV) and fast recombination rate of photo generated electron-hole pairs. As a result, it can only absorb short-wavelength ultraviolet light and have low utilization of visible light energy, which limited its practical application.

To narrow the band gap of TiO₂, many methods have been considered, such as metal or non-metal element doping, dye sensitization, mixture other compound and so on [22,24,25]. For the past few years, noble metal doping has been studied to enhance photocatalytic activity due to its excellent resistance of oxidation, localized surface plasmon resonance (LSPR) effect and improved fast separation rate of electron-holes [26,27], such as Au, Ag, Pt and Pd [28]. The photocatalytic activity of BiPO₄ nano-rods was much improved by the decoration of Au-Pd bimetallic alloy so that the trichloroethylene was successfully degraded under visible light illumination [29]. Weon et al. studied Pt and fluoride co-modified TiO₂ as a deactivation-resistant photocatalyst for the degradation of VOC. The surface Pt could much improve the generation of reactive oxygen species (ROS) since Pt could act as charge acceptor so that photo generated holes could fast react with adsorbed

* Corresponding author.

E-mail address: jygong@hust.edu.cn (J. Gong).

¹ These authors contributed equally to this work.

water to generate more $\cdot\text{OH}$ [30]. In fact, the noble metal NPs could form an intermediary for trapping or transferring photo-generated electrons [31].

In addition, morphology change is also an important method to improve photocatalytic property of catalyst [32]. It has been proved that the fluorescence wavelength, photoluminescence quantum yields and their lifetime would be improved by growing an epitaxial-type shell of another semiconductor [33], such as CdSe@CdS [34], $\text{TiO}_2\text{@MoS}_2$ [35], $\text{Fe}_3\text{O}_4\text{@Au}$, etc. Hollow structure has been attracted much attention because of its high specific surface area and abundant active reaction sites. Besides, light will be refracted and scattered many times in the hollow inner cavity, so as to reduce the diffusion distance of electron-hole pairs and maximize the utilization of sunlight [36].

For further improve the photocatalytic performance of catalyst, yolk-shell structure, which contains the core inside a void space surrounded by a semiconductor shell, has been developed. This structure includes the advantages of both core-shell structure and hollow structure. Au@TiO_2 yolk-shell NPs have been utilized in photocatalytic or photoelectrocatalytic fields. 3D-array of Au-TiO_2 yolk-shell performed a higher photocatalytic activity on H_2 generation than Au-TiO_2 [37]. The higher activity was due to the elongation of light path length because of the multiscattering in-between Au-TiO_2 and the reflection inside of TiO_2 shell. Du et al. prepared Au@TiO_2 hollow submicrospheres with controllable sizes and shell thicknesses by hydrothermal method [38]. The obtained Au@TiO_2 hollow submicrospheres exhibited a 30% increase compared with that of P25 TiO_2 . However, there are few reports on photocatalytic oxidation of VOCs by Au decorated TiO_2 and related mechanism, and the effect of different nanomaterials structure on photocatalytic oxidation efficiency of VOCs is unclear yet.

In this work, core-shell and yolk-shell structure with Au as the core and TiO_2 as the shell were respectively synthesized to explore their performance on photocatalytic degradation of VOCs and stability under visible light illumination. Their physical and chemical properties were systematically evaluated. We also analyzed the mechanism of photocatalytic oxidation of VOCs by means of free radical detection. And the mechanism of the influence of catalyst structure on its photocatalytic effect was also discussed.

2. Experimental section

2.1. Materials

CTAB (A.R., $\geq 99.0\%$), NaHCO_3 (A.R., $\geq 99.5\%$), ascorbic acid (A.R., $\geq 99.7\%$), TiCl_3 (A.R., 15.0–20.0%), NaCl (A.R.), glucose (A.R.), absolute ethanol (A.R., $\geq 99.7\%$), TBOT (C.P., $\geq 98.0\%$), ammonium hydroxide (A.R., 25–28%) and NaBH_4 ($\geq 98.0\%$) were all obtained from Sinopharm Chemical Reagent Co., Ltd. (Shanghai, China). $\text{HAuCl}_4\cdot 3\text{H}_2\text{O}$ ($\geq 99.9\%$) and Poly(sodium-p-styrenesulfonate) (PSS, average Mw 70,000) were obtained from Aladdin Bio-Chem Technology Co., Ltd. (Shanghai, China). The ultrapure water used throughout the experiment had a resistivity of 18.2 $\text{M}\Omega\text{ cm}$.

2.2. Synthesis of core-shell Au@TiO_2

2.2.1. Synthesis of Au NPs

Procedures of synthesizing core-shell Au@TiO_2 were illustrated in Scheme 1A. The gold NPs with diameter of about 25 nm were prepared by seed-growth method [39]. Gold seed solution was obtained by reducing HAuCl_4 by NaBH_4 . Briefly, 0.6 ml of NaBH_4 solution (0.01 M) was added into the mixture contained 0.25 ml of HAuCl_4 solution (0.01 M) and 7.5 ml of CTAB solution (0.1 M) under stirring. The solution was stirred continuously for 5 min and kept at 27 °C for 2 h. Next was the preparation of the growth solution. Specifically, 6.4 ml of CTAB solution, 0.8 ml of HAuCl_4 solution and 3.8 ml of ascorbic acid solution (0.1 M) were added into 32 ml of deionized water successively. The resultant solution changed from yellow to colorless when shaken

evenly. At last, the seed solution (0.04 ml) was added into the growth solution dropwise and the mixture was shocked until the color of solution began to change and then kept at room temperature for 12 h to form Au NPs.

2.2.2. Synthesis of core-shell Au@TiO_2

The as-synthesized Au NPs were encapsulated by 10 ml of PSS solution (2 g/L, 6 mM NaCl solution as solvent). The concentration of PSS is related to the self-growth process of TiO_2 [40]. Typically, 10 ml of as-synthesized Au NPs solution was centrifuged to remove the excess CTAB and re-dispersed into 10 ml of water. Then it was added into the PSS solution drop by drop. The duration time of PSS adsorption process was 4 h and then maintained for another 4 h. After centrifuging the mixture to removed excess PSS, the PSS-encapsulated Au NPs were re-dispersed into water.

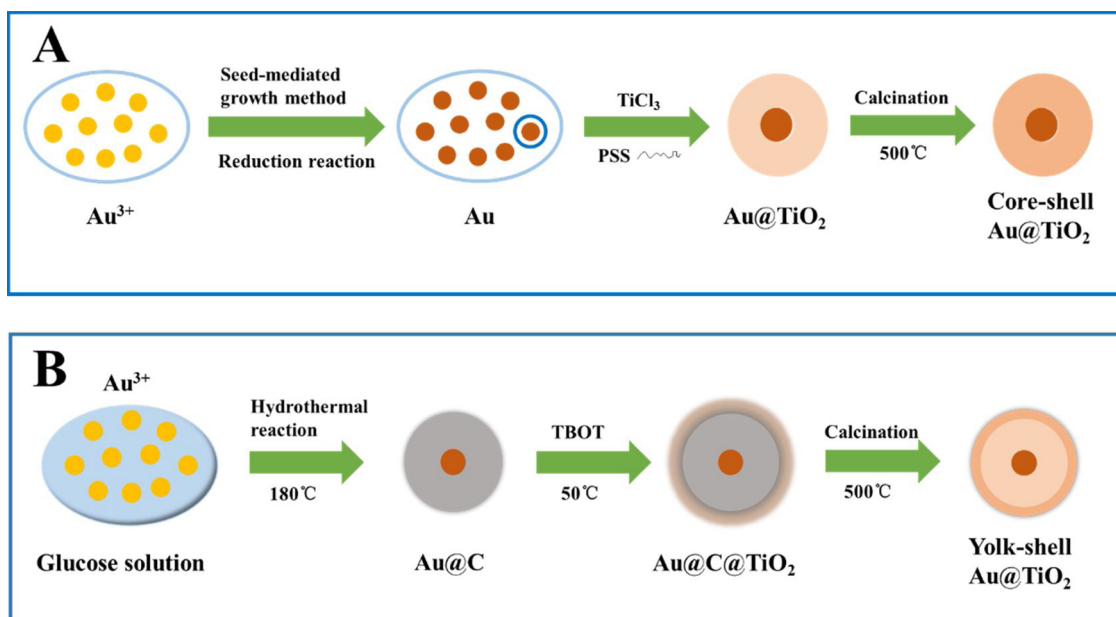
TiCl_3 (1.72 ml, 0.86 ml, 0.57 ml and 0.43 ml for Au loads of 0.07, 0.14, 0.21, 0.28 at%, respectively) as the precursor of TiO_2 was added into 8 ml of water under stirring, and then the saturated NaHCO_3 solution (6 ml, 3 ml, 2 ml, 1.5 ml, respectively) was added dropwise. When the solution get darker, the PSS-encapsulated Au NPs were added into it immediately. After stirring continuously for 30 min, the product was washed by centrifugation for several times and dried at 80 °C for 10 h. Finally, it was calcined at 500 °C for 4 h to form anatase TiO_2 . The synthesized core-shell Au@TiO_2 with different Au loads were defined as 0.07Au@ TiO_2 -CS, 0.14Au@ TiO_2 -CS, 0.21Au@ TiO_2 -CS and 0.28Au@ TiO_2 -CS, respectively. TiO_2 spheres were synthesized in the same way without Au NPs.

2.3. Synthesis of yolk-shell Au@TiO_2

Carbon sphere was employed as the template to prepare yolk-shell Au@TiO_2 as described in Scheme 1B. Core-shell Au@C spheres were prepared by a one-step hydrolysis method via the following steps: 4.5 g of glucose was dissolved in 30 ml of deionized water and 25 mM of HAuCl_4 solution (0.2 ml, 0.4 ml, 0.6 ml and 0.8 ml for Au loads of 0.07, 0.14, 0.21, 0.28 at%, respectively) was then added with continues stirring for 30 min. The formative clear solution was transferred to a 50 ml Teflon autoclave and treated at 180 °C for 12 h. The resultant products were washed with deionized water and ethanol for several times and dried at 80 °C for 10 h. Then, 0.5 g of dried core-shell Au@C templates were dispersed in 100 ml of ethanol, followed by adding 0.3 ml of ammonia solution. After stirring for 30 min, 0.5 ml of TBOT was added into the above solution dropwise and the reaction was kept stirring for 4 h at 50 °C. The resulting solution was washed several times with deionized water and ethanol, and dried at 80 °C for 10 h to obtain Au@C@TiO_2 . Finally, the obtained powders were calcined at 500 °C in air for 4 h to remove carbon template. The synthesized yolk-shell Au@TiO_2 with different Au loads were named as 0.07Au@ TiO_2 -YS, 0.14Au@ TiO_2 -YS, 0.21Au@ TiO_2 -YS and 0.28Au@ TiO_2 -YS, respectively. Hollow TiO_2 was synthesized in the same way without Au.

2.4. Materials characterization

The morphological and crystal structure of the samples were characterized by transmission electron microscopy (TEM, JEM-2100 F electron microscope operating at 200 kV), elemental mapping and HAADF-STEM imaging (FEI Tecnai G2 F30 microscope equipped with an EDAX energy-dispersive X-ray analysis system) and X-ray spectroscopy (XRD, 2θ ranges from 10° to 80°, using a diffractometer at 40 kV and 40 mA). The chemical compositions were analyzed with X-ray photoelectron spectroscopy (XPS, conducted on a 5300 ESCA instrument (Perkin-Elmer PHI Co., USA) using an Al $K\alpha$ X-ray source at a power of 250 W). The UV–vis diffuse reflection spectra (UV–vis DRS) was obtained for the dry-pressed disk samples by using a Scan UV–vis spectrophotometer (UV-2600, Shimadzu) with 100% BaSO_4 as a reference. The N_2 adsorption-desorption isotherms were measured on



Scheme 1. Schematic illustration of the procedure of synthesizing (A) core-shell Au@TiO_2 , (B) yolk-shell Au@TiO_2 NPs.

Quadrascorb SI analyzer at 77 K. The specific surface area, pore volume, and pore size were calculated based on Brunauer-Emmett-Teller (BET) analyses at the degassing temperature was 150°C for 3 h. Electron spin resonance (ESR) spectra was obtained with a Bruker EPR A300 spectrometer at room temperature with or without visible light illumination.

2.5. Photocatalytic experiments

The degradation of gaseous toluene under visible light irradiation was conducted in a sealed quartz reactor. The catalyst was flattened evenly at the bottom of the reactor and stirred with a mixer to equalize the gas. A 300 W Xe lamp with a cut-off filter of 400 nm was fixed above the reactor. The light energy was around $1.35\text{ mW}/\text{cm}^2$. A certain concentration of gaseous toluene was injected into the reactor for photocatalytic experiments at room temperature and pressure. Without special declaration, the concentration of gaseous toluene is 80 ppmv (equal to 300 ppm) and the dosage of catalyst is 5 mg. The concentration of gaseous toluene was analyzed by gas chromatography (FULI GC9790 Plus).

2.6. Photoelectrochemical measurements

The photoelectrochemical properties were examined at room temperature using a CHI 660E electrochemistry work station in Na_2SO_4 (0.1 M) solution with a three-electrode system. Platinum plate and AgCl/Ag electrode (saturated with KCl) worked as the counter electrode and the reference electrode, respectively. The FTO substrate (F doped SnO_2 transparent conductive glass) with photocatalysts were used as the working electrode. Typically, 10 mg of the samples was dispersed in a mixture solution contain 200 μL of deionized water, 200 μL of absolute ethyl alcohol and 50 μL of Nafion. 10 μL of the above suspension liquid was dropped onto the FTO conductive glass with exposure fixed area of 1 cm^2 . The light source is the same with the photocatalytic degradation of gaseous toluene mentioned above.

3. Results and discussion

TEM and HRTEM images of $\text{Au@TiO}_2\text{-CS}$ and $\text{Au@TiO}_2\text{-YS}$ were shown in Fig. 1A–B and Fig. 1D–F. Both $\text{Au@TiO}_2\text{-CS}$ and $\text{Au@TiO}_2\text{-YS}$ showed a similar morphology of Au core encased by TiO_2 shell.

Whereas, there was an obvious cavity inside of the TiO_2 shell shown in Fig. 1E. The diameter of $\text{Au@TiO}_2\text{-CS}$ NPs and Au@C@TiO_2 NPs were about 525 nm and 375 nm, respectively. As carbon disappeared gradually in the calcining process, the TiO_2 shell layer of Au@C@TiO_2 shrinks slightly inward, thus the particle size of the $\text{Au@TiO}_2\text{-YS}$ slightly reduce to about 350 nm. And the diameter of Au core was expanded from approximately 25 nm to 70 nm~90 nm. It could be explained that Au NPs expanded after calcining without external binding, which lead to a larger particle size [41,42]. The lattice fringes of $\text{Au@TiO}_2\text{-CS}$ and $\text{Au@TiO}_2\text{-YS}$ NPs (Fig. 1B and F) were both 0.352 nm, corresponding to (1 0 1) crystal plane of anatase TiO_2 . The composition of $\text{Au@TiO}_2\text{-CS}$ and $\text{Au@TiO}_2\text{-YS}$ was further verified by HAADF-STEM imaging and elemental mapping (Fig. 1C for $\text{Au@TiO}_2\text{-CS}$ and Fig. 1G for $\text{Au@TiO}_2\text{-YS}$). It confirmed that there was only one Au NP uniformly distributing in $\text{Au@TiO}_2\text{-CS}$ or $\text{Au@TiO}_2\text{-YS}$, and it was located in the inner of TiO_2 shell.

XRD patterns of as-synthesized $\text{Au@TiO}_2\text{-CS}$ and $\text{Au@TiO}_2\text{-YS}$ samples with different Au contents were shown in Fig. 2. Obviously, two kinds of diffraction peaks can be found for all $\text{Au@TiO}_2\text{-CS}$ NPs (Fig. 2A) and $\text{Au@TiO}_2\text{-YS}$ (Fig. 2B) NPs with different Au contents, respectively representing anatase TiO_2 (black star) and face-centered cubic Au (red triangles). The intensity of TiO_2 peaks was relatively small because of the high intensity of Au in Fig. 2A. In addition, Au peaks intensity became stronger while the peaks intensity of TiO_2 became weaker as the Au content increase. Fig. 2B showed that the locations and intensities of $\text{Au@TiO}_2\text{-YS}$ XRD patterns are similar with that of $\text{Au@TiO}_2\text{-CS}$, indicating that the yolk-shell structure had no obvious effect on the crystal phase. Moreover, the crystal growth orientation of Au changed to a certain extent due to the effect of heat treatment [41,43]. In the XRD patterns, the Au (2 2 0) crystal surface was more exposed than Au (1 1 1), which is different from the standard card JCPDS 04-0784 (Fig. S1). In order to verify that this transformation is related to the thermal treatment, we synthesized the 0.14 Au/ TiO_2 composite, in which Au NPs were reduced by NaBH_4 and deposited on the anatase TiO_2 surface. The XRD pattern of Au/ TiO_2 (Fig. S1) was more close to the standard card. So, we speculated that the crystal surface change was related to the thermal treatment.

The N_2 adsorption desorption isotherms of $\text{Au@TiO}_2\text{-CS}$ and $\text{Au@TiO}_2\text{-YS}$ were shown in Fig. 3. Clearly, there was a typical type IV isotherm with a hysteresis loop at high-pressure region, indicating the mesoporous structure of the samples [44]. It is obvious that $\text{Au@TiO}_2\text{-}$

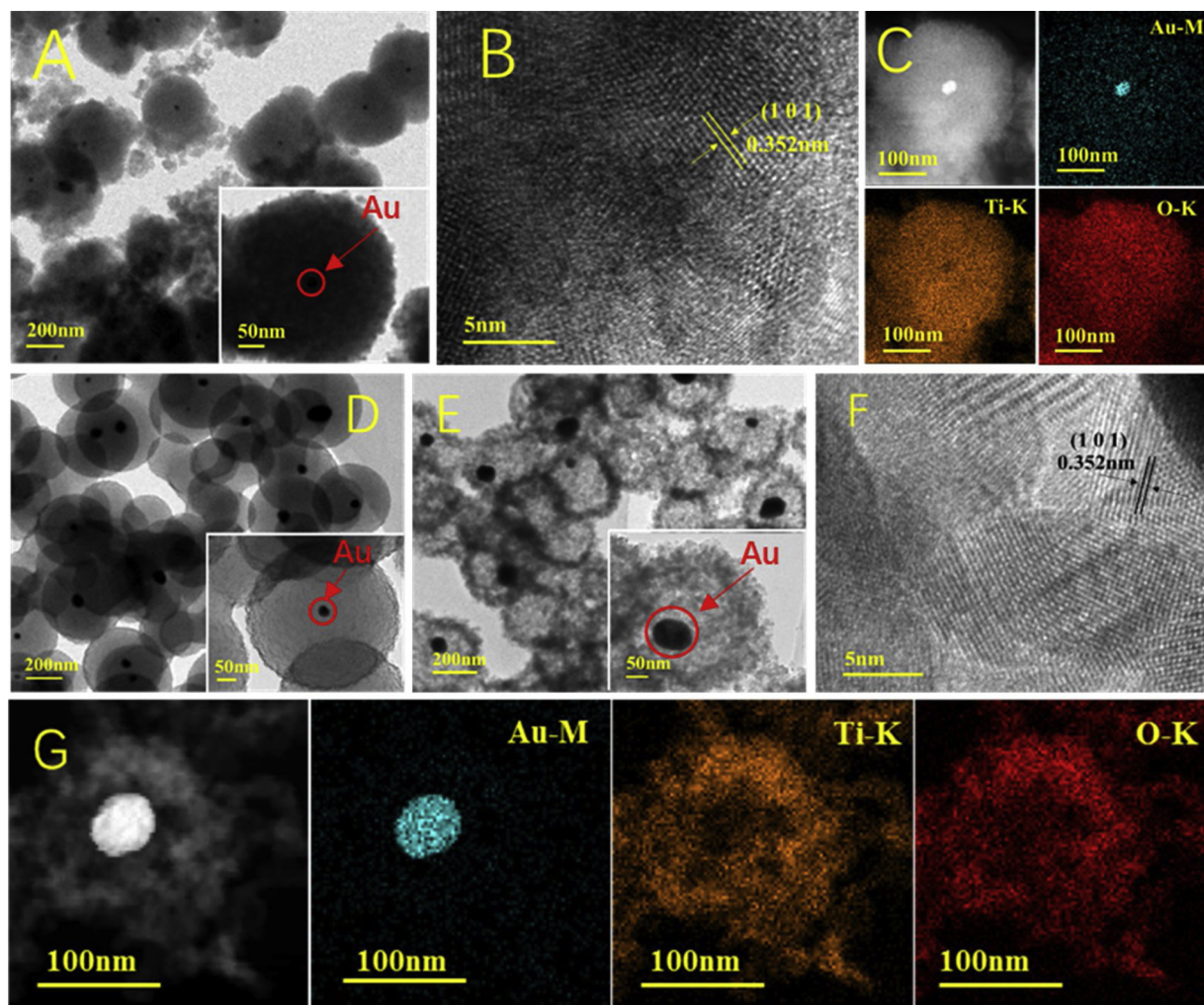


Fig. 1. (A) TEM, (B) HRTEM, (C) HAADF-STEM and element mappings of Au, Ti, O of Au@TiO₂-CS. (D) TEM of Au@C@TiO₂. (E) TEM, (F) HRTEM, (G) HAADF-STEM and element mappings of Au, Ti, O of Au@TiO₂-YS.

YS exhibited a more excellent adsorption and desorption capacity, and the BET specific surface area of Au@TiO₂-YS was 128.9 m²/g, which was 3.78 times higher than that of Au@TiO₂-CS (34.1 m²/g). At the same time, pore volume and average pore size of Au@TiO₂-YS were also larger than that of Au@TiO₂-CS. Pore size distribution (Fig. S2) also showed a high content of mesoporous particles in Au@TiO₂-YS, which would act as the path of gas exchange between the internal cavity of the catalytic and the external environment to enhance the

degradation effect.

Optical properties of the different samples were measured by diffuse reflectance UV–vis absorbance spectra. Fig. 4A showed that Au@TiO₂-YS sample performed the best absorption property due to secondary adsorption of reflect light caused by the unique structure. Clearly, both Au@TiO₂-CS and Au@TiO₂-YS samples have a broad absorption feature at about 570 nm due to the LSPR effect [45], but Au@TiO₂-YS performed stronger absorption. These plasma metal nanocrystals had very

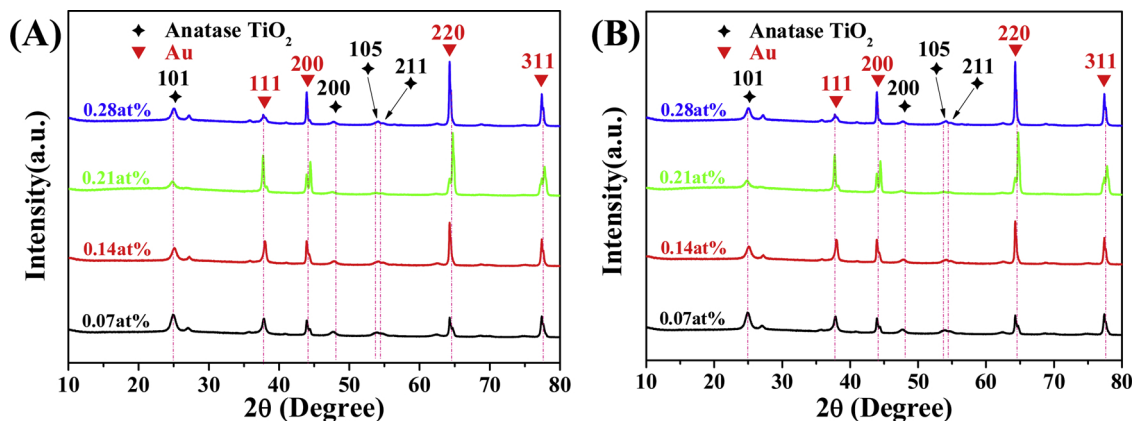


Fig. 2. XRD patterns of (A) Au@TiO₂-CS and (B) Au@TiO₂-YS.

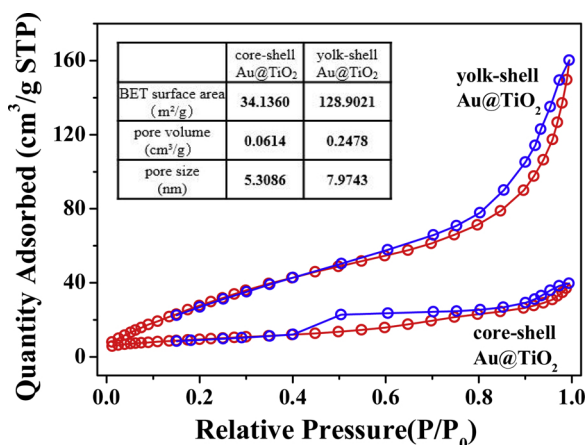


Fig. 3. N₂ adsorption-desorption isotherms of Au@TiO₂-CS and Au@TiO₂-YS.

large absorption and scattering cross-sections that strongly focus light near the metal surface, leading to an enhanced light absorption of TiO₂ by means of scattering, absorption enhancement, sensitization and thermal electron injection [46]. Moreover, the different particle size, shape and the dielectric constant of the surrounding medium of loaded Au on Au@TiO₂-CS and Au@TiO₂-YS induced the different light absorption intensity [47–49]. The band gaps of semiconductors were calculated according to Kubelka-Munk method [50], as shown in Fig. 4B. The extrapolated band gap energy of Au@TiO₂-CS and Au@TiO₂-YS were 2.86 eV and 2.75 eV, respectively, both lower than that of pure anatase TiO₂ (~2.95 eV), implying the excellent photocatalytic activity of Au@TiO₂-YS.

XPS was employed to characterize the elements of as-prepared different samples. The survey spectra (Fig. 5A) indicated that all of them were predominantly composed of Ti, O, C and Au. The Ti 2p XPS spectra of Au@TiO₂-CS and Au@TiO₂-YS observed in Fig. 5B can be respectively fitted into four peaks centered at 458.52, 458.99, 464.09, 464.80 eV and 457.77, 458.23, 463.43, 463.90 eV, which can be attributed to the binding energies of Ti³⁺ 2p_{3/2}, Ti⁴⁺ 2p_{3/2}, Ti³⁺ 2p_{1/2} and Ti⁴⁺ 2p_{1/2}, respectively [51]. And the Ti 2p of pure TiO₂ spheres and hollow TiO₂ shown in Fig. S3 also had similar fitting peaks. These results suggested that there exist not only Ti⁴⁺ but also Ti³⁺.

The O 1s peaks of the XPS spectra were asymmetrical illustrated in Fig. 5C. Both spectra of Au@TiO₂-CS and Au@TiO₂-YS could be decomposed into two characteristic peaks, a primary peak at lower binding energy corresponding to Ti–O bond [52], and a weaker contribution assigned to –OH surface hydroxyl groups [53] at higher energy. The adsorption oxygen included chemical adsorption oxygen and physical adsorption oxygen. The increase of adsorption oxygen

indicated promoting of the adsorption of oxygen species and it was favorable for photocatalytic reaction. On the one hand, chemical adsorption of oxygen species such as surface hydroxyl could trap photo-generated hole, which can generate ·OH. On the other hand, physical adsorption of oxygen species such as O₂ could accept photo-generated electron to accelerate the generation of ·O₂[–].

The binding energy of Au 4f_{7/2} and 4f_{5/2} were 82.9 eV and 86.4 eV (ΔE = 3.5 eV) in Fig. 5D, respectively. There was a little shift towards the direction of lower binding energy compared with standard Au 4f_{7/2} at 84.0 eV, indicating that it showed the characteristics of electron acceptors [54]. There were two main reasons for the shift. One was because of the quantum size effect of Au NPs. The second one was due to the strong interaction between Au and TiO₂. There was almost no Au 4f signal in Au@TiO₂-CS but a slight signal was observed in Au@TiO₂-YS. This is because that Au NPs were loaded in the interior of TiO₂ shell and the TiO₂ shell of Au@TiO₂-CS was much thicker than that of Au@TiO₂-YS.

The photocatalytic properties of as-prepared photocatalysts were evaluated by photocatalytic degradation of high concentration of gaseous toluene (80 ppmv) under visible light illumination. Fig. 6A showed that the degradation efficiency of gaseous toluene on Au@TiO₂-CS first increased to 35% with the Au content increased to 0.14 at% but slightly decreased while further increase Au concentration from 0.14 at% to 0.28 at%. Too much Au may lead to the accumulation and uneven dispersion of gold, reducing the activity of catalyst. However, lower Au content will produce inadequate active centers on catalyst surface. It was also clear that the degradation efficiency of gaseous toluene over Au@TiO₂-YS was much higher than that of Au@TiO₂-CS at the same Au content, as shown in Fig. 6B. The best degradation efficiency achieved almost 57% over 0.14 Au@TiO₂-YS. It may be due to the increased secondary absorption of refraction and reflection of light happened inside the shell, which leads to the enhancement of LSPR effect and utilization of light [37]. In the meantime, bulk recombination of photo generated e[–] and h⁺ would be restrained when TiO₂ shell got much thinner [38]. In addition, the hollow interior and porous TiO₂ shell of the yolk-shell structure provided larger surface area and more channels compared with that of Au@TiO₂-CS NPs, facilitating the adsorption and diffusion of reaction substrates, which contribute to higher gaseous toluene degradation efficiency [55,56].

The effect of different catalyst dosage on the degradation of gaseous toluene was also evaluated. The degradation efficiency and reaction rate were certain improved with the catalyst dosage multiples, as shown in Fig. 6C. 2.5 mg of catalyst is even too little to cover the bottom of the reactor and 10 mg is too much. Herein, 5 mg was selected as the optimal amount of catalyst for further trials. Fig. 6D showed the effect of gaseous toluene concentration on degradation efficiency. In the range of concentration of gaseous toluene tested in our experiment, clearly, the degradation efficiency decreased with the increase of gaseous toluene

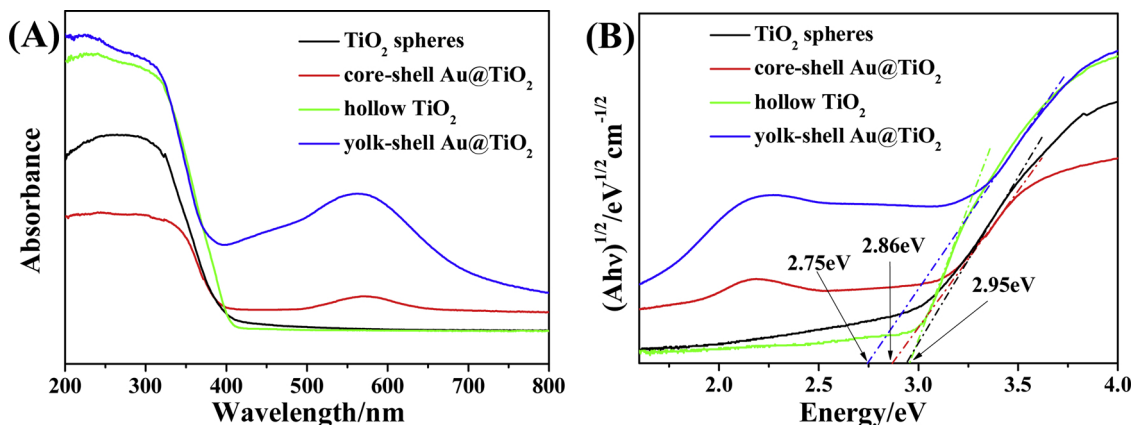


Fig. 4. (A) UV-vis absorbance spectra, (B) plots of $(\alpha h\nu)^{1/2}$ versus E (eV) for TiO₂ spheres, hollow TiO₂, Au@TiO₂-CS and Au@TiO₂-YS.

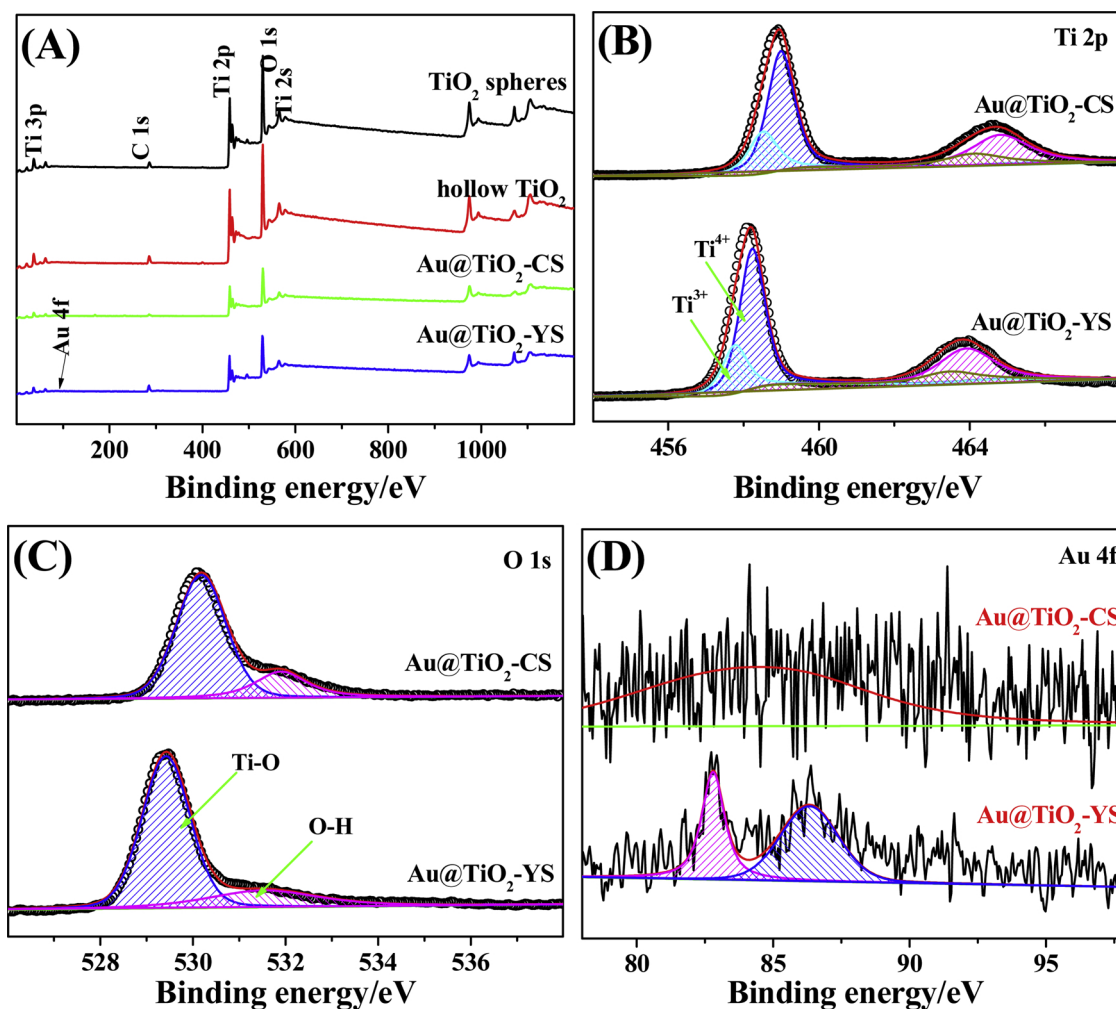


Fig. 5. XPS patterns of (A) survey spectrum, (B) Ti 2p, (C) O 1s, (D) Au 4f.

concentration. The reason for this phenomenon may be that the lower initial concentration of gaseous toluene is, the more opportunities they contact with the photocatalyst, and the faster degradation rate will be. Furthermore, to evaluate the stability of these photocatalysts, 0.14 $\text{Au@TiO}_2\text{-CS}$ and 0.14 $\text{Au@TiO}_2\text{-YS}$ were respectively selected to conduct gaseous toluene recycling degradation experiments, as shown in Fig. 6E and F. As can be seen from the experimental results, the adsorption amount of gaseous toluene in dark could be ignored compared with that in the photocatalytic degradation process. Moreover, as $\text{Au@TiO}_2\text{-YS}$ has a larger BET surface area, the adsorption capacity in dark of $\text{Au@TiO}_2\text{-YS}$ for gaseous toluene is slightly higher than that of $\text{Au@TiO}_2\text{-CS}$. Furthermore, both of the $\text{Au@TiO}_2\text{-CS}$ and $\text{Au@TiO}_2\text{-YS}$ performed excellent stability during three continuous circles.

To further understand the effect of different structure on photo-generated charge separation and electron transfer process, the photo-electrochemical measurements were carried out on pure TiO_2 spheres, hollow TiO_2 , $\text{Au@TiO}_2\text{-CS}$ and $\text{Au@TiO}_2\text{-YS}$. As shown in Fig. 7, $\text{Au@TiO}_2\text{-YS}$ exhibited a higher photocurrent density under visible light illumination than that of $\text{Au@TiO}_2\text{-CS}$ and other different structures of TiO_2 . Moreover, the photocurrent density of hollow TiO_2 is also higher than pure TiO_2 spheres, both of which proved that the hollow structure could promote the charge separation rate and utilization of light.

Electron spin resonance (ESR) was used to measure the generated radicals during the photocatalytic process and the defect on photocatalyst. Fig. 8A showed that both $\text{Au@TiO}_2\text{-CS}$ and $\text{Au@TiO}_2\text{-YS}$ had obvious TEMPO-h^+ peaks in the dark condition. Moreover, these

characteristic peaks became weaker under visible light illumination, and peaks of $\text{Au@TiO}_2\text{-YS}$ decreased faster than $\text{Au@TiO}_2\text{-CS}$. It suggested that h^+ was gradually exhausted due to its direct participation in photocatalytic degradation reaction, and it involved a faster reaction rate in $\text{Au@TiO}_2\text{-YS}$. As depicted in Fig. 8B and C, the characteristic peaks of $\text{DMPO}\cdot\text{OH}$ and $\text{DMPO}\cdot\text{O}_2^-$ were detected and the signal strength increased with the increase of irradiation time. At the same time, it showed that the production of both $\cdot\text{OH}$ and $\cdot\text{O}_2^-$ over $\text{Au@TiO}_2\text{-YS}$ were faster than that of $\text{Au@TiO}_2\text{-CS}$, indicating that $\text{Au@TiO}_2\text{-YS}$ performed a good separation effect on photo-generated e^- - h^+ pairs so that more free radicals would be generated compared with $\text{Au@TiO}_2\text{-CS}$ under the same conditions. Fig. 8D showed a broad signal at $g = 1.999$ for all samples, which could be unequivocally assigned to a paramagnetic Ti^{3+} center in a distorted oxygen ligand field caused by the surface oxygen vacancies [57,58]. And the amount of Ti^{3+} increased with the light irradiation as shown in Fig. S4. The small amount of Ti^{3+} in pure TiO_2 spheres and $\text{Au@TiO}_2\text{-CS}$ could come from the precursor of TiCl_3 [59]. To verify this conclusion, a new experiment was conducted by using TiCl_4 to replace TiCl_3 as the precursor for the synthesis of TiO_2 spheres and core-shell Au@TiO_2 . The results shown in Fig. S5 indicated that there was almost no Ti^{3+} in TiO_2 spheres (TiCl_4). There was a little amount of Ti^{3+} in core-shell Au@TiO_2 (TiCl_4) but it was fewer than that in core-shell Au@TiO_2 (TiCl_3). It suggested that the small amount of Ti^{3+} could from TiCl_3 . Meanwhile, the existence of Au would also form Ti^{3+} species during the calcination process [51,60]. In addition, incomplete oxidation of carbon may occur in the process of removing carbon templates in thermal treatment due to the lack of air,

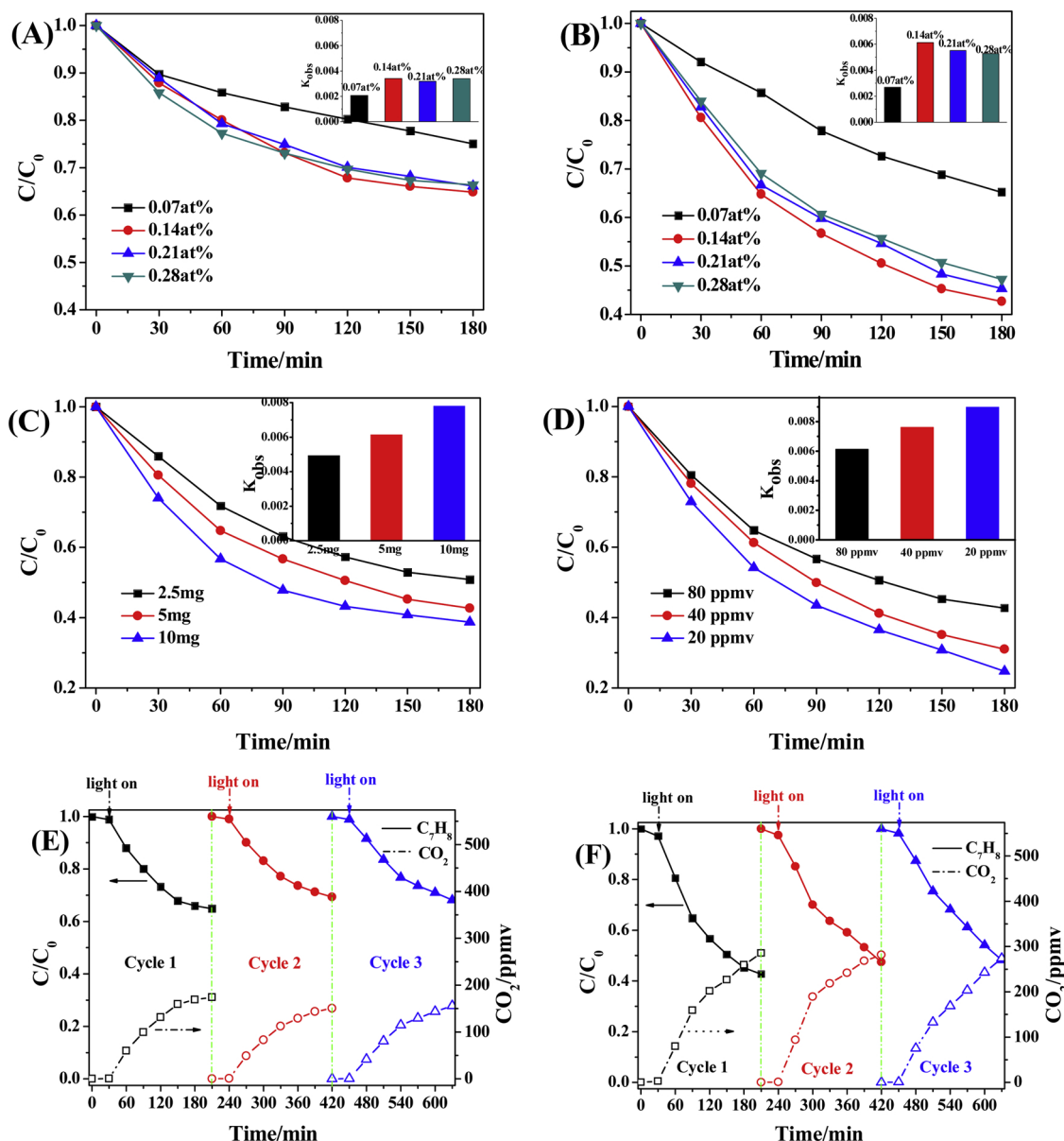


Fig. 6. Photocatalytic activities under visible light of as-prepared samples: C_7H_8 photodegradation with different (A) Au content in $Au@TiO_2$ -CS and (B) $Au@TiO_2$ -YS, (C) catalyst dosage of $Au@TiO_2$ -YS and (D) C_7H_8 concentration. The cycling test of (E) $Au@TiO_2$ -CS and (F) $Au@TiO_2$ -YS.

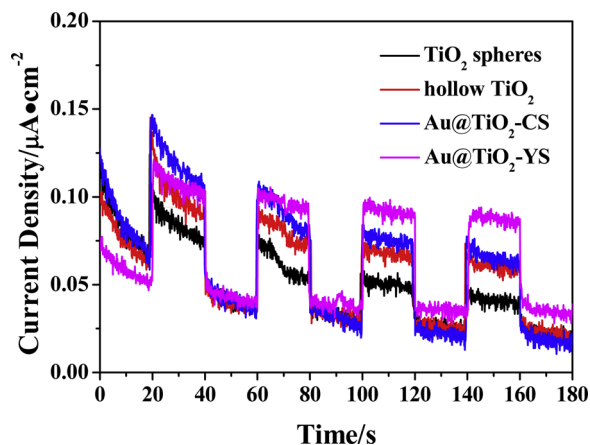


Fig. 7. Photocurrent generation under pulsed irradiation for TiO_2 spheres, hollow TiO_2 , $Au@TiO_2$ -CS and $Au@TiO_2$ -YS.

resulting in a small amount of Ti^{3+} in TiO_2 coating [61]. Therefore, there were some Ti^{3+} in the hollow TiO_2 and $Au@TiO_2$ -YS [49]. Au NPs could interact strongly with the TiO_2 carrier, and the electrons photo-excited from VB to Ti^{3+} states would transfer to Au [62], resulting in Au showing the characteristics of electrons acceptors [54]. $Au@TiO_2$ -YS had many channels that could promote the contact between O_2 and Au NPs, so that it could accelerate the rate of electron captured by adsorbed oxygen [63].

The generated h^+ , $\cdot OH$, $\cdot O_2^-$ and Ti^{3+} were responsible for the achieved excellent photocatalytic activity over $Au@TiO_2$ -YS, resulting from the synthesized unique structure. The noble metal NPs can prevent the photo-generated electron from immediately recombining with the hole by receiving electrons transferred from the conductive band (CB) of TiO_2 and Ti^{3+} . It can also transfer electrons to oxygen molecules that are attached to the material surface to form more $\cdot O_2^-$ [54,64]. At the same time, $\cdot OH$ are also produced through oxidation of adsorbed H_2O by h^+ . These free radicals then rapidly oxidize the adsorbed gaseous toluene into CO_2 and H_2O by breaking the benzene ring, and the

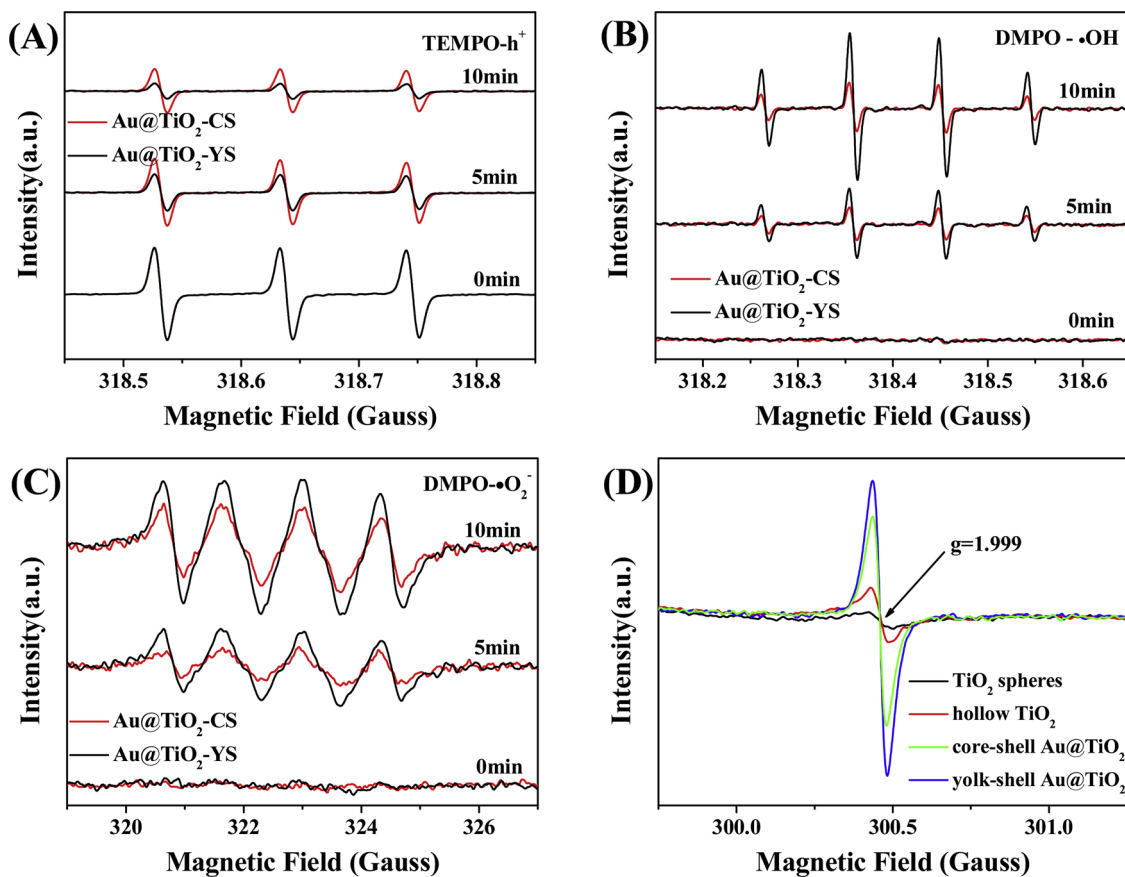
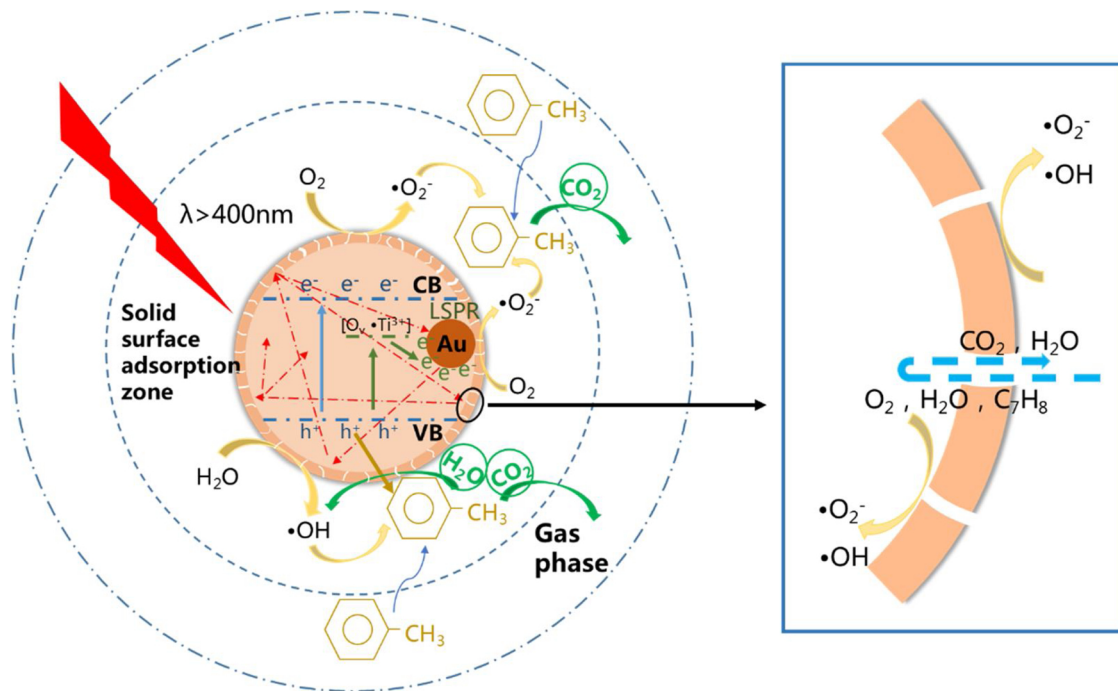


Fig. 8. ESR spectra of (A) TEMPO- h^+ , (B) DMPO- $\cdot OH$, (C) DMPO- $\cdot O_2^-$ for Au@TiO₂-CS and Au@TiO₂-YS and (D) Ti³⁺ for synthesized four samples.



Scheme 2. The photocatalytic degradation mechanism of Au@TiO₂-YS.

mechanism of the photocatalytic degradation enhancement of Au@TiO₂-YS was shown at the Scheme 2.

4. Conclusions

In conclusion, the yolk-shell Au@TiO₂ NPs with different Au loads that exhibited excellent performances of photocatalytic VOCs degradation under visible light illumination was successfully synthesized by a template removal method. The degradation efficiency of gaseous toluene by yolk-shell Au@TiO₂ is 1.63 times higher than that of core-shell Au@TiO₂ within 2 h. Except the LSPR effect of Au NPs and the formation of Schottky barrier between loaded Au NPs and TiO₂ interface, the reasons for the high photocatalytic degradation efficiency of gaseous toluene caused by yolk-shell Au@TiO₂ are as follows. Firstly, light could be reflected and refracted so many times in the cavity provided by the yolk-shell structure, which could improve light absorption, thus enhance the LSPR effect of Au and further narrow the binding energy. Secondly, thin TiO₂ shells and Ti³⁺ species can promote the separation efficiency of photo-generated e⁻-h⁺ pairs and the presence of Au NPs will facilitate this process further. Thirdly, yolk-shell Au@TiO₂ provides a huge specific surface area and numerous mesoporous channels, which can enhance the absorption of VOC and provide more active sites. The produced ROS, such as h⁺, ·OH and ·O₂⁻, are all responsible for the photocatalytic degradation process. In addition, the yolk-shell Au@TiO₂ catalysts performed good stability after three rounds of recycling. Thus, the design of noble metal doped yolk-shell structure provides a new perspective for the fabrication of photocatalyst on remediation of indoor gaseous pollutant.

Conflict of interest

There are no conflicts to declare.

Acknowledgements

This project was supported by the National Natural Science Foundation of China (Grant No. 21707038) and Hubei Provincial Natural Science Foundation of China (Grant No. 2017CFB668). The authors wish to thank the Analytical and Testing Center of HUST for the use of XRD, TEM, and BET equipment.

Appendix A. Supplementary data

Supplementary material related to this article can be found, in the online version, at doi:<https://doi.org/10.1016/j.apcatb.2019.03.056>.

References

- [1] B.F. Yu, Z.B. Hu, M. Liu, H.L. Yang, Q.X. Kong, Y.H. Liu, *Int. J. Refrig.* 32 (2009) 3–20.
- [2] A. Chaudhary, S. Hellweg, *Environ. Sci. Technol.* 48 (2014) 14607–14614.
- [3] J. Palau, M. Colomer, J.M. Penya-Roja, V. Martínez-Soria, *Ind. Eng. Chem. Res.* 51 (2012) 5986–5994.
- [4] B. Liu, X. Li, Q. Zhao, J. Liu, S. Liu, S. Wang, M. Tade, *J. Mater. Chem. A* 3 (2015) 15163–15170.
- [5] A. Šuligoj, U.L. Štanger, A. Ristić, M. Mazaj, D. Verhovšek, N.N. Tušar, *Appl. Catal. B* 184 (2016) 119–131.
- [6] L. Xue, T. Wang, J. Gao, A. Ding, X. Zhou, D.R. Blake, X. Wang, S. Saunders, S. Fan, H.C. Zuo, Q.Z. Zhang, W.X. Wang, *Atmos. Chem. Phys. Discuss.* 13 (2013) 27243–27285.
- [7] R.-J. Huang, Y. Zhang, C. Bozzetti, K.-F. Ho, J.-J. Cao, Y. Han, K.R. Daellenbach, J.G. Slowik, S.M. Platt, F. Canonaco, P. Zotter, R. Wolf, S.M. Pieber, E.A. Brun, M. Crippa, A. Piazzalunga, M. Schwikowski, G. Abbaszade, J. Schnelle-Kreis, R. Zimmermann, Z. An, S. Szidat, U. Baltensperger, I.E. Haddad, A.S.H. Prevôt, *Nature* 514 (2014) 218.
- [8] J.E. Krechmer, M.M. Coggon, P. Massoli, T.B. Nguyen, J.D. Crounse, W. Hu, D.A. Day, G.S. Tyndall, D.K. Henze, J.C. Rivera-Rios, J.B. Nowak, J.R. Kimmel, R.L. Mauldin, H. Stark, J.T. Jayne, M. Sipilä, H. Junninen, J.M. St. Clair, X. Zhang, P.A. Feiner, L. Zhang, D.O. Miller, W.H. Brune, F.N. Keutsch, P.O. Wennberg, J.H. Seinfeld, D.R. Worsnop, J.L. Jimenez, M.R. Canagaratna, *Environ. Sci. Technol.* 49 (2015) 10330–10339.
- [9] R. Fang, H. Huang, J. Ji, M. He, Q. Feng, Y. Zhan, D.Y. Leung, *Chem. Eng. J.* 334 (2018) 2050–2057.
- [10] H. Huang, H. Huang, Q. Feng, G. Liu, Y. Zhan, M. Wu, D.Y. Leung, *Appl. Catal. B* 203 (2017) 870–878.
- [11] J. Ji, Y. Xu, H. Huang, M. He, S. Liu, G. Liu, R. Fang, *Chem. Eng. J.* 327 (2017) 490–499.
- [12] J. Kim, P. Zhang, J. Li, J. Wang, P. Fu, *Chem. Eng. J.* 252 (2014) 337–345.
- [13] M. Djurendic-Brenes, G. Stojiljkovic, V. Pilija, J. Forensic Sci. 61 (2016) 875–878.
- [14] B. Guieysse, C. Hort, V. Platel, R. Munoz, M. Ondarts, S. Revah, *Biotechnol. Adv.* 26 (2008) 398–410.
- [15] J. Palau, M. Colomer, J.M. Penya-Roja, V. Martínez-Soria, *Ind. Eng. Chem. Res.* 51 (2012) 5986–5994.
- [16] S. Weon, W. Choi, *Environ. Sci. Technol.* 50 (2016) 2556–2563.
- [17] G. Zhang, Q. Xiong, W. Xu, S. Guo, *Appl. Clay Sci.* 102 (2014) 231–237.
- [18] S. Wang, H.M. Ang, M.O. Tade, *Environ. Int.* 33 (2007) 694–705.
- [19] A.H. Mamaghani, F. Haghighat, C.-S. Lee, *Appl. Catal. B* 203 (2017) 247–269.
- [20] J. Gong, C. Yang, W. Pu, J. Zhang, *Chem. Eng. J.* 167 (2011) 190–197.
- [21] Z. Shayegan, C.-S. Lee, F. Haghighat, *Chem. Eng. J.* 334 (2018) 2408–2439.
- [22] J. Gong, W. Pu, C. Yang, J. Zhang, *Catal. Commun.* 36 (2013) 89–93.
- [23] J. Shi, Y. Kuwahara, T. An, H. Yamashita, *Catal. Today* 281 (2017) 21–28.
- [24] T. Barakat, V. Idakiev, R. Cousin, G.S. Shao, Z.Y. Yuan, T. Tabakova, S. Siffert, *Appl. Catal. B* 146 (2014) 138–146.
- [25] K.C. Christoforidis, S.J.A. Figueroa, M. Fernández-García, *Appl. Catal. B* 117–118 (2012) 310–316.
- [26] S.W. Zhang, B.P. Zhang, S. Li, X.Y. Li, Z.C. Huang, *J. Alloy. Compd.* 654 (2016) 112–119.
- [27] P. Fu, P. Zhang, *Appl. Catal. B* 96 (2010) 176–184.
- [28] M. Wen, K. Mori, Y. Kuwahara, H. Yamashita, *ACS Energy Lett.* 2 (2017) 1–7.
- [29] Y. Zhang, S.-J. Park, *J. Catal.* 355 (2017) 1–10.
- [30] S. Weon, J. Kim, W. Choi, *Appl. Catal. B* 220 (2018) 1–8.
- [31] S.I. Mogal, V.G. Gandhi, M. Mishra, S. Tripathi, T. Shripathi, P.A. Joshi, D.O. Shah, *Ind. Eng. Chem. Res.* 53 (2014) 5749–5758.
- [32] H. Tong, S. Ouyang, Y. Bi, N. Umezawa, M. Oshikiri, J. Ye, *Adv. Mater.* 24 (2012) 229–251.
- [33] L.J. Lauhon, M.S. Gudiksen, D. Wang, C.M. Lieber, *Nature* 420 (2002) 57.
- [34] X. Peng, M.C. Schlamp, A.V. Kadavanich, A.P. Alivisatos, *J. Am. Chem. Soc.* 119 (1997) 7019–7029.
- [35] R. Dai, A. Zhang, Z. Pan, A.M. Al-Enizi, A.A. Elzatahry, L. Hu, G. Zheng, *Small* 12 (2016) 2792–2799.
- [36] M. Gao, L. Zhu, W.L. Ong, J. Wang, G. Wei Ho, *Catal. Sci. Technol.* 5 (2015) 4703–4726.
- [37] X. Shi, Z. Lou, P. Zhang, M. Fujitsuka, T. Majima, *ACS Appl. Mater. Interfaces* 8 (2016) 31738–31745.
- [38] J. Du, J. Qi, D. Wang, Z. Tang, *Energy Environ. Sci.* 5 (2012) 6914–6918.
- [39] H. Chen, L. Shao, Y.C. Man, C. Zhao, J. Wang, B. Yang, *Small* 8 (2012) 1503–1509.
- [40] C. Fang, H. Jia, S. Chang, Q. Ruan, P. Wang, T. Chen, J. Wang, *Energy Environ. Sci.* 7 (2014) 3431–3438.
- [41] H. Pan, S.H. Ko, C.P. Grigoropoulos, *J. Heat Transfer* 130 (2008) 092404–092404-092407.
- [42] A. Corma, H. Garcia, *Chem. Soc. Rev.* 37 (2008) 2096–2126.
- [43] S. Arcidiacono, N.R. Bieri, D. Poulikakos, C.P. Grigoropoulos, *Int. J. Multiphase Flow* 30 (2004) 979–994.
- [44] M. Kruk, M. Jaroniec, *Chem. Mater.* 13 (2001) 3169–3183.
- [45] D. Buso, J. Pacifico, A. Martucci, P. Mulvaney, *Adv. Funct. Mater.* 17 (2007) 347–354.
- [46] P.K. Jain, X. Huang, I.H. El-Sayed, M.A. El-Sayed, *Acc. Chem. Res.* 41 (2008) 1578–1586.
- [47] R. Zanella, S. Giorgio, C.-H. Shin, C.R. Henry, C. Louis, *J. Catal.* 222 (2004) 357–367.
- [48] E. Kowalska, O.O.P. Mahaney, R. Abe, B. Ohtani, *Phys. Chem. Chem. Phys.* 12 (2010) 2344–2355.
- [49] A. Primo, A. Corma, H. Garcia, *Phys. Chem. Chem. Phys.* 13 (2011) 886–910.
- [50] C. Ye, Y. Bando, G. Shen, D. Golberg, *J. Phys. Chem. B* 110 (2006) 15146–15151.
- [51] N. Kruse, S. Chenakin, *Appl. Catal. A* 391 (2011) 367–376.
- [52] X. Liu, Z. Xing, Y. Zhang, Z. Li, X. Wu, S. Tan, X. Yu, Q. Zhu, W. Zhou, *Appl. Catal., B* 201 (2017) 119–127.
- [53] S. Zhang, W. Pu, H. Du, Y. Wang, C. Yang, J. Gong, *Appl. Surf. Sci.* 459 (2018) 363–375.
- [54] S. Arrif, F. Morfin, A.J. Renouprez, J.-L. Rousset, *J. Am. Chem. Soc.* 126 (2004) 1199–1205.
- [55] W. Zhang, G. Li, H. Liu, J. Chen, S. Ma, T. An, *Environ. Sci. Nano* (2019).
- [56] H. Sun, Q. He, P. She, S. Zeng, K. Xu, J. Li, S. Liang, Z. Liu, *J. Colloid Interface Sci.* 505 (2017) 884–891.
- [57] J. Huo, Y. Hu, H. Jiang, C. Li, *Nanoscale* 6 (2014) 9078–9084.
- [58] X. Feng, P. Wang, J. Hou, J. Qian, Y. Ao, C. Wang, *J. Hazard. Mater.* 351 (2018) 196–205.
- [59] Y. Zhou, C. Chen, N. Wang, Y. Li, H. Ding, *J. Phys. Chem. C* 120 (2016) 6116–6124.
- [60] S. Lee, C. Fan, T. Wu, S.L. Anderson, *Surf. Sci.* 578 (2005) 5–19.
- [61] L. Hao, K. Miyazawa, H. Yoshida, Y. Lu, *Mater. Res. Bull.* 97 (2018) 13–18.
- [62] X. Xin, T. Xu, J. Yin, L. Wang, C. Wang, *Appl. Catal. B* 176–177 (2015) 354–362.
- [63] H. Wang, T. An, A. Selloni, *J. Chem. Phys.* 146 (2017) 184703.
- [64] N. Siemer, A. Lützen, M. Zolner, J. Frenzel, D. Muñoz-Santibañero, A. Savitsky, W. Lubitz, M. Muhler, D. Marx, J. Strunk, *J. Am. Chem. Soc.* 140 (2018) 18082–18092.